IEEE Robotics and Automation Letters (RA-L) paper, presented at ICRA 2026, Vienna, Austria. Cite as RA-L paper.

A Novel Upper Limb Rehabilitation Framework Based on Dual-Arm Robotics for Therapist-Like Traction Training

Gao Lin[1], Fei Wang[1], and Shuai Han[2]

***Abstract*—In this letter, we propose a novel upper limb rehabilitation framework based on dual-arm robotics for therapist-like traction training. Prioritizing patient safety, an 8-DOF kinematic model of the upper limb is derived to evaluate the reachable workspace of the palm center and proximal forearm during interaction with a dual-arm robot. Leveraging the characteristics of dual-arm rehabilitation, a non-redundant inverse kinematics method is proposed to constrain joint angles, thereby establishing a safety mechanism under dual constraints. Secondly, considering the training science and compliance, a potential field control strategy is introduced to enable the robot to learn the therapist's traction characteristics from a single demonstration. Combined with the leader-follower control, it reproduces the therapist's assistance and allows for compliant interaction. Experimental results show that the proposed framework combines the strong adaptability and comfort of end-effector robots with the precise rehabilitation of exoskeleton robots. As dual-arm and humanoid robots become more widely adopted, the proposed scheme holds promise for delivering therapist-like safe, scientific, and compliant rehabilitation in clinical and home settings.**

***Index Terms*—dual-arm rehabilitation, therapist-like traction, upper limb kinematics, learning from demonstration.**

I. Introduction

STROKE is the second leading cause of death and disability globally [1]. More than 75% of stroke survivors suffer from upper limb dysfunction, resulting in loss of independence and increased burden on families [2]. Traditional upper limb rehabilitation relies on therapists performing traction training on the affected limb with both arms. While this approach is safe, scientific, and compliant, it suffers from low repeatability and places a heavy workload on therapists [3]. With advances in robotics, upper limb rehabilitation robots have emerged as an effective solution for assisting patient recovery [4].

Upper limb rehabilitation robots are categorized into two types: end-effector and exoskeleton robots. The former uses an end-effector to apply traction to the patient's hand for training. End-effector robots have the advantages of strong adaptability, simple wearing, safety and comfort, and a wide range of motion. For example, Han *et al.* [5] propose an assist-as-needed strategy for an end-effector robot, enabling training to adapt to subjects with varying motor abilities. Chen *et al.* [6] propose an end-effector robot motion learning framework that can provide compliant response and personalized training as the subject's motor ability changes. Related studies also include [7] and [8]. However, end-effector robots cannot precisely control individual joints, making it particularly difficult to maintain the correct upper-limb posture during spatial training. Therefore, most end-effector robots adopt low-DOF planar training to ensure safety. The exoskeleton is worn directly on the upper limb and controls each joint individually to provide precise rehabilitation. For example, Jun *et al.* [9] propose the NESM-γ exoskeleton, which enables precise training of the shoulder and elbow. Yves *et al.* [10] design the ANYexo exoskeleton, which offers accurate control of upper limb joints and allows subjects to perform precise spatial training. However, the high-DOF and flexibility of the upper limb make exoskeleton robots structurally complex, difficult to control and wear, less adaptable to different patients, and prone to generating additional interaction forces and torques due to high human-robot coupling. Therefore, how to combine the advantages of end-effector and exoskeleton rehabilitation robots while overcoming their limitations to provide adaptable, low-contact, and precise high-DOF training for the affected limb is an important topic worth exploring.

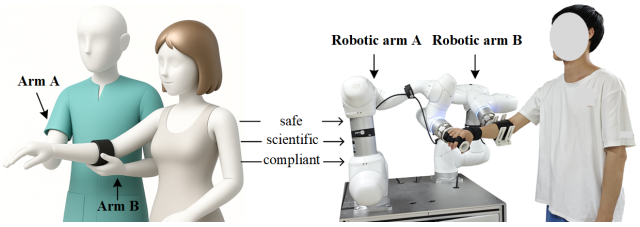

Fig. 1. Dual-arm emulation of therapist traction realizes therapist-like training.

In traditional upper limb rehabilitation, therapists deliver traction training to the affected limb using both arms. Inspired by this, we hypothesize that dual-arm or humanoid robots can replace the therapist's arms to provide therapist-like training. Recent studies on dual-arm and humanoid robots that imitate human operations support our hypothesis. In human-object-robot collaboration, Ovur *et al.* [11] employ multi-sensor fusion to achieve natural handover of objects between human hands and a dual-arm robot. Doganay *et al.* [12] propose an adaptive framework where a human and a dual-arm robot collaboratively carry heavy objects, similar to two humans working together. In terms of human-like fine manipulation,

This work was supported in part by the National Natural Science Foundation of China under Grant 62373087, in part by the Liaoning Provincial Applied Basic Research Program under Grant 2025JH2/101300009, and in part by the Liaoning Revitalization Talents Program under Grant XLYC24110114. *(Corresponding author: Fei Wang and Shuai Han).*

This work involved human subjects or animals in its research. Approval of all ethical and experimental procedures and protocols was granted by the Northeastern University, Human Participants Ethics Committee under Application No. NEU-EC-2025B058S.

[1]Gao Lin and Fei Wang are with the Faculty of Robot Science and Engineering, Northeastern University, Shenyang 110000, China 2310767@stu.neu.edu.cn; wangfei@mail.neu.edu.cn

[2]Shuai Han is with the Department of Neurosurgery, Shengjing Hospital of China Medical University, Shenyang 110000, China hanshuai19870217@outlook.com

IEEE Robotics and Automation Letters (RA-L) paper, presented at ICRA 2026, Vienna, Austria. Cite as RA-L paper.

Fan *et al.* [13] propose a learning-based framework for a dual-arm robot to manipulate objects skillfully while maintaining tight coordination. Wang *et al.* [14] deploy a dual-arm robot in factory settings to imitate and replace worker in performing collaborative and precise object placement tasks. In addition, several studies apply dual-arm robots to manipulate flexible materials in 2-D and 3-D space, allowing for bending into specified shapes, just like human operation [15], [16]. In summary, dual-arm robots are capable of precise spatial manipulation, which addresses a key limitation of current end-effector rehabilitation robots and highlights an advantage of exoskeletons. However, current dual-arm research primarily focuses on human-like collaboration in human-object-robot or robot-object scenarios, where human involvement is indirect. In contrast, upper-limb rehabilitation requires close physical human-robot interaction (pHRI). Moreover, most existing studies imitate human external behaviors while overlooking the emulation of internal dynamics. Given these differences, emulation learning is more appropriate than imitation learning for rehabilitation training involving pHRI. Accordingly, this work shifts from current human-like collaboration (imitation learning) to therapist-like rehabilitation (emulation learning) tasks, aiming to achieve robot therapist-like safe, scientific, and compliant interaction.

In this work, we propose a dual-arm robotic upper-limb rehabilitation framework that emulates therapist traction. Given the close pHRI in upper-limb rehabilitation, safety is prioritized, followed by personalization and compliance. The main contributions of this work are as follows:

- Rehabilitation strategy: A novel framework for upper-limb rehabilitation is proposed, utilizing a dual-arm robot to effectively integrate the advantages of both end-effector and exoskeleton rehabilitation robots.
- Safety mechanism: An accurate upper limb kinematic model is established, combined with the characteristics of dual-arm rehabilitation to design a dual-constraint safety mechanism in task and joint spaces.
- Human-robot interaction: A potential field control strategy is introduced in learning-from-demonstration, combined with leader-follower control to emulate the therapist's scientific and compliant interaction.

II. Safety Mechanism

A. Upper Limb Kinematics

To meet the high safety demands of rehabilitation, an accurate 8-DOF kinematic model of the upper limb is established. As shown in Fig. 2, the sternoclavicular joint (1-DOF) allows the scapula to perform protraction and retraction. The shoulder joint (3-DOF) permits arm rotation, abduction/adduction, and flexion/extension. The elbow joint (1-DOF) enables elbow flexion/extension. The wrist joint (3-DOF) allows wrist pronation/supination, flexion/extension and abduction/adduction.

The base frame $H_0 = [x_0\ y_0\ z_0]$ is located at the sternoclavicular joint. The local frames $H_{1-7} = [x_i\ y_i\ z_i, i = 1, ..., 7]$ are fixed at joint $i+1$. The end-point frame $H_8 = [x_8\ y_8\ z_8]$ is located at the center of the palm. l_1, l_2, l_3, l_4, l'_3, and l''_3 represent the acromiohumeral interval, the upper arm length, the forearm length, the distance from the wrist to the palm center, the distance from the elbow to p_{a2} (end-effector B), and the distance from p_{a2} to the wrist, respectively. As shown in Table I, the kinematic parameters of the upper limb are established according to the standard Denavit-Hartenberg (D-H) convention. The definitions of the standard D-H parameters θ_i, a_i, d_i, α_i, and the transformation matrix $T_i^{i-1}(q)$ can be found in [17]. The vector $q = [\theta_1, ..., \theta_8]^T \in \mathbb{R}^{8\times1}$ denotes the joint variables. For the above model, a point $p_j = [x_j\ y_j\ z_j\ 1]$ defined in frame j can be represented in the base frame as

$$p_j^0 = \prod_{i=1}^{j} \left[T_i^{i-1}(q_i)\right] p_j = T_j^0(q) p_j. \tag{1}$$

Therefore, $p_{a1} = [x_{a1}\ y_{a1}\ z_{a1}]$ and $p_{a2} = [x_{a2}\ y_{a2}\ z_{a2}]$ can be represented in the base frame H_0 as

$$\begin{bmatrix} x_{a1} & y_{a1} & z_{a1} \end{bmatrix}^T = T_8^0(q_1) \begin{bmatrix} 0 & 0 & 0 & 1 \end{bmatrix}^T, \tag{2}$$

$$\begin{bmatrix} x_{a2} & y_{a2} & z_{a2} \end{bmatrix}^T = T_4^0(q_2) \begin{bmatrix} 0 & l'_3 & 0 & 1 \end{bmatrix}^T, \tag{3}$$

where T_8^0 and $T_4^0 \in \mathbb{R}^{4\times4}$ are defined in equation (1). $q_1 = q \in \mathbb{R}^{8\times1}$ and $q_2 = [\theta_1, ..., \theta_4]^T \in \mathbb{R}^{4\times1}$. Given the upper limb poses p_{a1} and p_{a2} expressed as functions of joint angles, dual safety constraints are constructed by leveraging the complementarity of task and joint space safety.

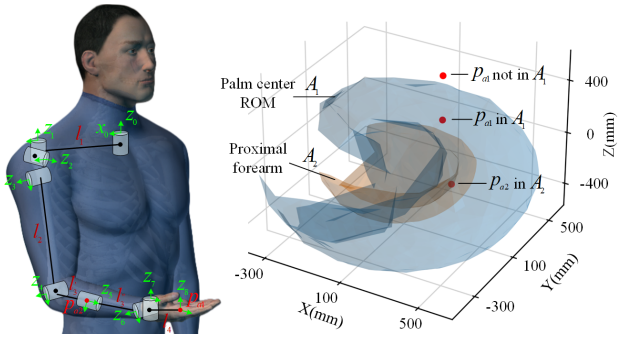

Fig. 2. The 8-DOF kinematic model and reachable workspace construction.

TABLE I
D-H Parameters For The 8-Dof Upper Limb Model

Joints	θ_i	a_i	d_i	α_i	Joint limits
scapula protraction	θ_1	l_1	0	0	-15−10
shoulder rotation	θ_2	0	0	90	-90−80
shoulder abduction	θ_3-90	0	0	-90	0−90
shoulder flexion	θ_4	l_2	0	0	-60−90
elbow flexion	θ_5 / θ_5+90	0 / l'_3	0	-90	-90−45
wrist supination	θ_6	0	l_3/ l''_3	-90	-90−0
wrist flexion	θ_7-90	0	0	90	-80−50
wrist abduction	θ_8	l_4	0	0	-15−45

B. Dual Safety Constraints

1) Task space constraints: From the perspective of global coordination, any motion that exceeds the reachable workspace leads to abnormal inter-joint coordination. Task space constraints can restrict the motion of specific segmental points along the upper limb to prevent non-physiological postures, such as excessive stretching or twisting. Based on the 8-DOF

IEEE Robotics and Automation Letters (RA-L) paper, presented at ICRA 2026, Vienna, Austria. Cite as RA-L paper.

kinematic model, the reachable training space of p_{a1} and p_{a2} is calculated using the Monte Carlo method.

$$E_1 = \left\{ p_{a1} \middle| T_8^0 \left(\sum_{i=1}^{N} q_1^i \right) \begin{bmatrix} 0 & 0 & 0 & 1 \end{bmatrix}^T \right\}, \quad (4)$$

$$E_2 = \left\{ p_{a2} \middle| T_4^0 \left(\sum_{i=1}^{N} q_2^i \right) \begin{bmatrix} 0 & l_3' & 0 & 1 \end{bmatrix}^T \right\}. \quad (5)$$

Here, E_1 and $E_2 \in \mathbb{R}^{3\times N}$ represent the solution spaces of p_{a1} and p_{a2}. First, we perform Delaunay triangulation on sets E_1 and E_2. Then, a parameter ε is defined to remove triangles with side lengths shorter than $1/\varepsilon$. Next, the filtered triangles are connected to generate the corresponding Alpha shapes (reachable workspaces) A_1 and A_2, as shown in Fig. 2. Finally, the ray-casting method is employed to determine whether p_{a1} and p_{a2} are within A_1 and A_2. Algorithm 1 summarizes the process of task space constraints.

Algorithm 1 Task space constraints.

Input: p_{a1}, p_{a2}, ε, and kinematic model
Output: True (p_{a1} in A_1 and p_{a2} in A_2) or False
$E_1, E_2 \leftarrow$ According to equations (4) and (5)
$A_1, A_2 \leftarrow$ Construct Alpha shapes with Delaunay and ε
for $i = 1, 2$ **do**
  count$\leftarrow$ Calculate intersections between p_{ai} and A_i
  If count is odd **then**
    Return True //p_{ai} in A_i, continue training
    Repeat steps $3-6$
  else
    Return False // Stop training

2) Joint space constraints: Even when the global motion remains within the reachable workspace, an individual joint may still exceed its physiological load. Joint space constraints act precisely on each joint, ensuring that local movements align with human biomechanical constraints. The 8-DOF system is redundant, leading to non-unique inverse kinematics solutions and making it difficult to impose joint constraints during training. Based on a dual-arm framework, a simple and efficient non-redundant inverse kinematics solver is proposed. The 8-DOF system is decomposed into two subsystems with 5 and 3 DOFs (the D-H parameters of each subsystem are listed in Table I), and the inverse kinematics of each subsystem is solved separately. For the 5-DOF subsystem, the point p_{a2} is represented in the base frame H_0 as

$$p_{a2}^0 = T_4^0 p_{a2}^4 = T_B^0 p_{a2}^B, \quad (6)$$

where T_B^0 represents the transformation matrix from the base frame of robotic arm B (whose end-effector is at p_{a2}) to H_0.

For the 3-DOF subsystem, the point p_{a1} is represented in the local frame H_5 as

$$p_{a1}^5 = T_8^5 p_{a1}^8 = T_0^5 T_A^0 p_{a1}^A, \quad (7)$$

where T_A^0 represents the transformation matrix from the base frame of robotic arm A (whose end-effector is at p_{a1}) to H_0.

Based on the above relationship, 5-DOF and 3-DOF inverse kinematics models are constructed to achieve efficient and accurate joint constraint control in rehabilitation.

III. Emulating therapist interaction

In traditional rehabilitation, the therapist uses their arms to traction the affected limb, providing personalized, compliant, and safe training. In this process, therapists play the role of trajectory planning, assistance, and soft constraints. The proposed framework requires only one demonstration to learn this therapist-like interaction. This process is divided into two stages: traction demonstration and learning from demonstration. We aim for the dual-arm robot to emulate the therapist's traction characteristics from demonstration. Then, in the absence of the therapist, the robot provides the same personalized assistance and allows compliant and safe interaction. This interaction enables compliant motion around the training trajectory while maintaining soft constraints. Both soft constraints and task-joint space constraints (hard constraints) act simultaneously to ensure training safety.

A. Traction Demonstration

By replacing the therapist's arms with serial rigid robots, the nonlinear dynamics of the m-DOF serial robot can be expressed as

$$M(q)\ddot{q} + \left[\frac{1}{2}\dot{M}(q) + S(q,\dot{q}) \right] \dot{q} + g(q) = \tau + J^T(q) F_h, \quad (8)$$

in which $F_h = F_{in} + F_c$ and $F_{in} = F_{th} + F_{pa} + F_d$.

Where $q \in \mathbb{R}^m$ denotes the joint variables. The definitions of the fundamental dynamic parameters can be found in [18]. $F_h \in \mathbb{R}^6$ denotes the resultant force. F_h can be decomposed into the external force $F_{in} \in \mathbb{R}^6$ acting on the end-effector and the control force $F_c \in \mathbb{R}^6$ within the control system. F_{in} consists of F_{th}, F_{pa}, and F_d, which represent the therapist's traction force, the force applied by the affected limb, and the mounting stress from the sensor, respectively. During the demonstration phase, the therapist provides traction to guide the patient in completing the task, at which point $F_c = 0N$. The dynamic relationship between force and pose is as follows.

$$D_t \left(\dot{p} - \dot{p}_d \right) + K_t \left(p - p_d \right) = F_{in}. \quad (9)$$

$D_t \in \mathbb{R}^6$ and $K_t \in \mathbb{R}^6$ denote the robot's initial damping and stiffness. The difference between the actual pose p and the desired pose p_d defines the pose deviation, with its derivative $(\dot{p} - \dot{p}_d)$ indicating the velocity deviation. Treating p as the desired pose p_d and accumulating incremental pose updates enables the end-effectors to track the therapist's traction.

$$p_d^{t+1} = \left(\xi^t + \Delta\xi, \Delta q_{Rp} q_{Rp}^t \right), \quad (10)$$

where p_d^{t+1} denotes the desired pose for the next control cycle. The current position and its deviation are represented by $\xi^t = [x^t\ y^t\ z^t]$ and $\Delta\xi = [\Delta x\ \Delta y\ \Delta z]$, respectively. Similarly, the current orientation and its deviation are denoted by $q_{Rp}^t = [q_{Rx}^t\ q_{Ry}^t\ q_{Rz}^t]$ and $\Delta q_{Rp} = [\Delta q_{Rx}\ \Delta q_{Ry}\ \Delta q_{Rz}]$. The velocity Δv^t and pose deviation $\Delta p^{t+1} \in \mathbb{R}^6$ are computed as

$$\Delta v^t = 1/D_t \times \left(F_{in} - K_t \times \Delta p^t \right), \quad (11)$$

$$\Delta p^{t+1} = \Delta p^t + \Delta v^t \times T_c, \quad (12)$$

IEEE Robotics and Automation Letters (RA-L) paper, presented at ICRA 2026, Vienna, Austria. Cite as RA-L paper.

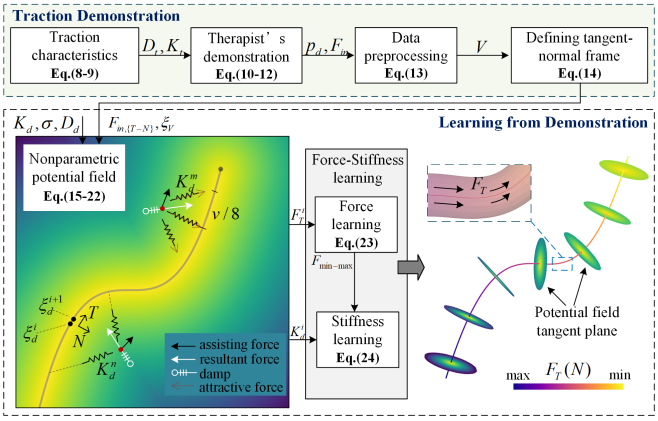

Fig. 3. Emulating the therapist's traction training from demonstration.

where T_c is the control period. During the demonstration, the pose $p_d \in \mathbb{R}^6$ and interaction force $F_{in} \in \mathbb{R}^6$ are recorded at a frequency of $1/T_c$ Hz. The collected dataset is downsampled into v uniformly spaced samples (attracting points) to construct the following dataset:

$$V = \left\{ \left[p_d^i; F_{in}^i \in \mathbb{R}^{6\times 1} \right] \in \mathbb{R}^{12\times 1} \right\}_{i=1}^{v} \in \mathbb{R}^{12\times v}. \tag{13}$$

$$\xi_d^i \leftarrow \min_{\xi_V^i \in V} \left\| \xi - \xi_V^i \right\|_2^2. \tag{14}$$

Define $\left\{T-N\right\}^i$ as the tangent-normal frame of the i-th attracting point. This frame is centered at attracting point $\xi_d^i \in \mathbb{R}^3$, with the tangent direction pointing toward the next attracting point ξ_d^{i+1}, and the normal direction oriented toward the current end-effector position $\xi \in \mathbb{R}^3$. The desired attracting point ξ_d^i is computed by minimizing the Euclidean distance between the current position ξ and the point set $\xi_V \in \mathbb{R}^{3\times v}$.

B. Learning from Demonstration

In the absence of the therapist, the robot provides the same personalized assistance as during the traction demonstration and allows compliant and safe interaction. A controller is designed by integrating the interaction characteristics extracted from the demonstration with a non-parametric potential field function [19]. At this stage, the control force F_c replaces the demonstration force F_{th} to provide equivalent assistance for upper limb movement. Accordingly, F_{in} and F_c are reformulated as $F_{in} = F_{pa} + F_d$ and $F_c = F_N + F_T$.

F_N and F_T represent the attractive force along the attracting point ξ_d^i and the propelling force toward the next attracting point ξ_d^{i+1}. F_N provides compliant constraints during training, while F_T provides assistance. To jointly generate tangent and normal forces applied at a current position, a non-parametric potential field is constructed by connecting the position of the end-effector to the corresponding attracting point ξ_d^i using a virtual spring with stiffness K_d^i. The potential energy of the i-th attracting point ξ_V^i at ξ is given by

$$\phi^i(\xi) = \phi_T^i(\xi) + \phi_N^i(\xi) = F_T^i(\xi) + \frac{K_d^i \left(\xi - \xi_V^i\right)}{2}. \tag{15}$$

Similar to gravitational attraction, the contribution of attractive forces should decrease as the distance between two points increases. Gaussian kernel functions are commonly used to measure the similarity between data points. We adopt a kernel regression approach to construct the total energy function based on the individual energy elements $\phi^i(\xi)$. At the current position ξ, the contribution of an energy element ξ_V^i is determined using a Gaussian kernel.

$$\omega^i(\xi) = e^{-\frac{1}{2\sigma^2}\left(\xi-\xi_V^i\right)^T\left(\xi-\xi_V^i\right)}. \tag{16}$$

The parameter σ determines the smoothness of the Gaussian kernel function and controls its bandwidth. When the attracting points are far apart, their mutual influence becomes negligible. To reduce computational load, improve online control speed, and smooth the attractive forces during continuous motion, we select the $v/8$ attracting points before and after ξ_d^i to compute the total potential energy (as shown in Fig. 3). Therefore, the total potential energy at ξ is given by

$$\Phi(\xi) = F_T^i(\xi) + \frac{\sum_{n=-v/8}^{v/8} \omega^{d+n}(\xi)\phi^{d+n}(\xi)}{\sum_{m=-v/8}^{v/8} \omega^{d+m}(\xi)}. \tag{17}$$

The attractive forces from the attracting points $\xi_{v/4+1}$ are normalized. The attractive coefficient of each point $\xi_{v/4+1}^i$ with respect to ξ is defined as

$$\tilde{\omega}^i(\xi) = \frac{\omega^i(\xi)}{\sum_{n=-v/8}^{v/8} \omega^{d+n}(\xi)}. \tag{18}$$

For attractive coefficient $\tilde{\omega}^i(\xi)$, there are two attributes: $0 < \tilde{\omega}^i(\xi) < 1$ and $\sum_{v/4+1} \tilde{\omega}^i(\xi) = 1$. Therefore, equation (17) can be simplified as

$$\Phi(\xi) = F_T^i(\xi) + \sum_{n=-v/8}^{v/8} \tilde{\omega}^{d+n}(\xi)\phi^{d+n}(\xi). \tag{19}$$

Similar to the energy dissipation principle of a damper-spring system, the energy dissipation field $\psi^i(\xi, \Delta\dot{\xi})$ can be considered to depend on the velocity deviation $\dot{e} = (\dot{\xi} - \dot{\xi}_d^i)$ at the current position ξ and the damping characteristics D_d^i.

$$\begin{aligned} \psi^i(\xi, \Delta\dot{\xi}) &= \psi_T^i\left(\xi, \dot{e}_T\right) + \psi_N^i\left(\xi, \dot{e}_N\right) \\ &= D_d^i \left[\left(\dot{\xi}_T - \dot{\xi}_{dT}^i \right) + \left(\dot{\xi}_N - \dot{\xi}_{dN}^i \right) \right]. \end{aligned} \tag{20}$$

Here, $\psi_T^i\left(\xi, \dot{e}_T\right)$ and $\psi_N^i\left(\xi, \dot{e}_N\right)$ represent the energy dissipation fields in the $\left\{T-N\right\}^i$ coordinate system. Therefore, the total dissipated energy $\Psi(\xi, \Delta\dot{\xi})$ is obtained through a weighted summation of the dissipation elements.

$$\Psi(\xi, \Delta\dot{\xi}) = \psi_T^i\left(\xi, \dot{e}_T\right) + \sum_{n=-v/8}^{v/8} \tilde{\omega}^{d+n}(\xi)\psi_N^{d+n}(\xi). \tag{21}$$

Thus, the total energy $E(\xi)$ at position ξ is given by

$$E(\xi) = \Phi(\xi) - \Psi(\xi, \Delta\dot{\xi}). \tag{22}$$

Returning to equation (15), we need to define $F_T^i(\xi)$ so that the affected limb receives the same assistance as in the demonstration. We hope that as the offset distance increases, the vertical potential field will dominate rather than $F_T^i(\xi)$, thereby reducing the safety risk caused by the assistance.

$$F_T^i(\xi) = \frac{2F_{in}^i}{1 + c^{\left\|\xi - \xi_d^i\right\|}}, \quad s.t.\ 1 \le c \le e. \tag{23}$$

IEEE Robotics and Automation Letters (RA-L) paper, presented at ICRA 2026, Vienna, Austria. Cite as RA-L paper.

The assistance width can be adjusted by the constant c to meet the training needs. In addition, we adjust K_d^i in equation (15) so that the robot can emulate the therapist's dynamic interaction stiffness. K_d^i is defined as

$$K_d^i = K_{\min} + (K_{\max} - K_{\min}) \frac{F_{in}^i - F_{in,\min}}{F_{in,\max} - F_{in,\min}}, \quad (24)$$

where $F_{in,min}$ and $F_{in,max}$ represent the minimum and maximum traction forces in set V. $K_{\min} = K_t - K_v$ and $K_{\max} = K_t + K_v$ define the limits of K_d, i.e., $K_d^i \in [K_{\min}, K_{\max}]$. Here, K_v is used to regulate the learning range of K_d.

In the experiments, we set $K_t = 150N/m$ and $K_v = 20N/m$ (corresponding to $K_d^i \in [130, 170]N/m$, which represents a moderate interaction level), with the associated $D_d^i \in [30, 50]N{\cdot}s/m$ and $D_t = 40N{\cdot}s/m$. The values of K_t, K_v and D_t can be adjusted according to the patient's motor ability (e.g., severe: $K_t = 200N/m$, $K_v = 10N/m$, and $D_t \in 50N{\cdot}s/m$; mild: $K_t = 100N/m$, $K_v = 30N/m$, and $D_t \in 30N{\cdot}s/m$) to balance the interactive performance and safety of the rehabilitation system.

C. Leader-follower Control

The therapist employs bimanual cooperative traction to achieve coordinated motion of the affected limb. Based on their assisting roles, the therapist's arms can be classified as the leader arm and the follower arm. The leader arm performs large-range traction tasks, functioning as a coarse adjustment, while the follower arm assists in correcting the motion post, functioning as a fine adjustment. During learning-from-demonstration, the desired pose $p_{dm}[\xi_{dm}^i, q_{dm}^i]$ associated with the current leader arm pose $p_m[\xi_m, q_m]$ is given by equation (14). The corresponding desired pose $p_{ds}[\xi_{ds}^i, q_{ds}^i]$ for the follower arm is inferred from the sampled set V. Therefore, the current pose $p_s[\xi_s, q_s]$ of the follower arm under the interaction force can be expressed as $p_s[\xi_{ds}^i + \Delta\xi_s, \Delta q_s * q_{ds}^i]$.

To avoid potential motion risks caused by stretching or squeezing of the arm, the distance d_{ms} between the end effectors should be within the distance d_p from the p_{a2} to p_{a1} under joint limits.

$$\begin{aligned} & d_p^2 = l_3^{''2} + l_4^2 + 2l_3^{''} l_4 \cos\theta_7 \cos\theta_8, \\ s.t. \quad & d_{p,|\theta_{\max}|}^2 \le d_{ms}^2 = ||\xi_m - {}^m\xi_s||^2 \le d_{p,|\theta_{\min}|}^2 \end{aligned} \quad (25)$$

where ${}^m\xi_s$ denotes the position of the follower arm's end-effector expressed in the base frame of the leader arm.

IV. Experiment and Result

A. Experiment Protocol

1) Dual-arm rehabilitation platform: As shown in Fig. 4(e), two Doosan M1509 cobots emulate the therapist's arms. Each is equipped with a six-axis force sensor (ATI Axia80) mounted at the end-effector for pHRI. The subject's upper limb is attached to the end-effector with training gloves and Velcro, ensuring comfort and ease of wear.

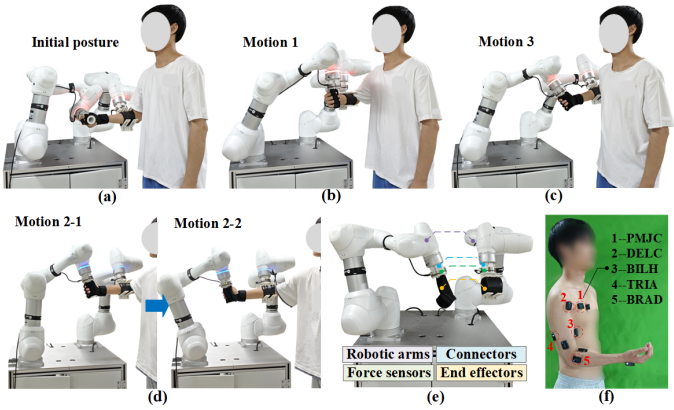

Fig. 4. Experimental schematic. (a-d) Illustrations of three training motions; (e) Dual-arm rehabilitation platform; (f) Placement of IMU and sEMG sensors. Muscles 1-5 correspond to the pectoralis major clavicular part (PMJC), deltoid clavicular part (DELC), biceps brachii long head (BILH), triceps brachii long head (TRIA), and brachioradialis (BRAD), respectively.

2) Experimental paradigm: Three multi-joint training motions are performed. As shown in Fig. 4(a–d), they are arm lifting, vertical chest expansion with rotational forward push (complex motion), and chest expansion. The first two motions are performed with robotic arm A as the leader arm, and the third with arm B as the leader. These motions simultaneously involve shoulder rotation (SR), shoulder flexion (SF), shoulder abduction (SA), elbow flexion (EF), wrist extension (WE), and wrist supination (WS). Eight male subjects (age: 23.5 ± 0.8 years old, weight: 67.6 ± 9.5kg, height: 175.2 ± 6.5cm, mean ± SD) take part in the experiment. In the beginning, the IMU and sEMG sensors will be attached to their body in the manner of Fig. 4(f) to collect upper limb angles and muscle activities. Then, the operator performs a traction demonstration on the subject. Finally, the robots will learn from demonstration and perform five reciprocating training sessions. This study was approved by the Northeastern University, Human Participants Ethics Committee (NEU-EC-2025B058S), and consents were obtained from the subjects.

B. Result

1) Effects of potential field parameters: Fig. 5 illustrates an example of the potential field corresponding to a reference trajectory under different parameters: K_d (in Eq. (15), controlling field intensity), σ (in Eq. (16), controlling field smoothness), and F_T (in Eq. (15), controlling traction force). The color represents the potential field intensity, while the arrows indicate its direction. From (a) to (b), the potential field becomes smoother as σ increases, but local details are diminished. This results in a blurrier field and causes underfitting to the desired trajectory. After testing, $\sigma = 0.2$ is selected for the experiments. From (a) to (c), as K_d decreases, the field intensity weakens, leading to increased compliance in the normal direction. However, an excessively small K_d reduces the soft constraint capability of the field, thereby improving safety risks. Therefore, adjusting K_d appropriately at different stages of training is essential for balancing safety and compliance. From (a) to (d), only F_T varies, directing the

IEEE Robotics and Automation Letters (RA-L) paper, presented at ICRA 2026, Vienna, Austria. Cite as RA-L paper.

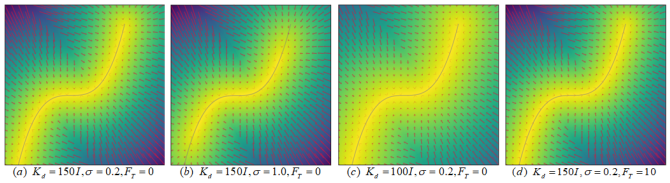

Fig. 5. Effects of parameter variations on the potential field.

traction toward the target point. Thus, tuning the magnitude or direction of F_T based on the patient's condition enables the design of targeted rehabilitation modes such as passive, semi-active, active, and resistive.

2) Joint constraints performance: This section aims to validate the performance of the proposed non-redundant inverse kinematics method in joint constraints. The reference joint angles, as shown in Fig. 6, involve coordinated movements of the shoulder, elbow, and wrist. A comparative evaluation is performed between the proposed non-redundant method and the 8-DOF redundant kinematic method (the basic method), using the Levenberg–Marquardt-based numerical optimization for inverse kinematics. The root mean square error (RMSE) serves as the evaluation metric.

The results show that the RMSE of the proposed method is zero on joints 1, 3, 5, 6, 7, and 8, and 0.08 on joints 2 and 4, which is much lower than the 5°–10° error tolerance routinely set for rehabilitation training, proving that our method is safe and effective. In contrast, the basic method exhibits significant errors across most joints. Notably, the RMSE reaches as high as 70.36 for joint 3 and 104.46 for joint 8, indicating a clear divergence in inverse kinematics solutions. Furthermore, the RMSE in joints 2, 3, 4, 7, and 8 exceeds 10. This level of error could misrepresent the patient's actual movements if applied directly in a rehabilitation system, leading to training interruptions or even injuries. From the perspective of error distribution, the basic method exhibits instability across multiple joints, primarily due to insufficient singularity handling and suboptimal utilization of redundant DOFs. The proposed method demonstrates superior global solving capability and convergence stability. It effectively constrains solution space deviations in the 8-DOF redundant system, maintaining continuity and controllability throughout the solving process. Therefore, our method can effectively reduce the frequency of unintended interruptions during rehabilitation, demonstrating improved stability and practical applicability of the rehabilitation system.

Real-time performance is also crucial in rehabilitation training, as the computation speed directly influences the smoothness of the interaction. Experimental results show that the proposed method achieves an average inverse kinematics solving time of $0.010s$ with Core i9-13900HX, outperforming the basic method's $0.016s$, with approximately 37.5% higher computational efficiency. These results indicate that the proposed method maintains high accuracy and offers enhanced real-time performance, contributing to improved quality of interaction and safety during rehabilitation training.

3) Dual-Arm traction effect: We compare the effects of the proposed scheme with the current end-effector method

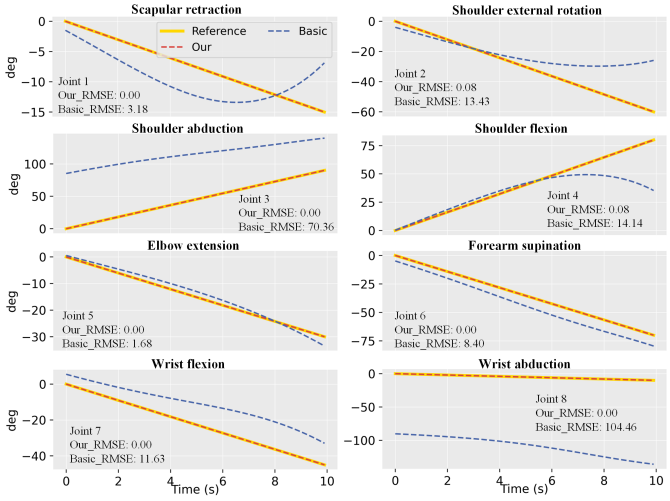

Fig. 6. Comparison of the proposed joint constraints method and the baseline.

TABLE II
PROPOSED FRAMEWORK VS. CURRENT END-EFFECTOR (SINGLE-ARM) AND MIME METHODS, WITH DEMONSTRATION TRAINING AS STANDARD

Method	Metrics	SR	SF	SA	EF	WE	WS
Motion 1	RMSE	0.90	1.55	0.91	2.01	0.96	0.97
Dual-Arm	PCC	0.99	0.97	0.99	0.99	0.99	0.99
Motion 1	RMSE	10.5	4.14	21.3	5.26	4.72	15.1
Single-Arm	PCC	0.93	0.57	0.95	0.99	0.59	0.99
Motion 1	RMSE	11.8	2.99	21.5	6.73	5.38	16.9
MIME	PCC	0.79	0.58	0.91	0.99	0.50	0.99
Motion 2	RMSE	1.05	2.41	0.81	1.93	1.45	0.89
Dual-Arm	PCC	0.98	0.99	1.00	0.99	0.99	1.00
Motion 2	RMSE	21.0	18.0	22.8	6.37	7.61	24.4
Single-Arm	PCC	-0.21	0.17	0.94	0.90	0.85	1.00
Motion 2	RMSE	23.1	14.7	22.6	4.83	9.05	26.7
MIME	PCC	-0.48	0.65	0.94	0.95	0.78	0.99
Motion 3	RMSE	0.89	1.55	0.86	1.77	1.42	0.91
Dual-Arm	PCC	0.99	0.99	1.00	0.99	0.92	0.99
Motion 3	RMSE	2.60	2.41	1.90	4.63	7.69	20.9
Single-Arm	PCC	0.98	0.99	0.99	0.99	0.05	-0.91

(with the leader arm performing the traction) [5], [6], [7] and the Mirror Image Movement Enabler (MIME) (with the arm A performing the traction, including Motions 1 and 2) [20]. Demonstration training is used as the reference, exhibiting performance comparable to that of a full-limb exoskeleton. These comparative experiments are conducted to verify whether the proposed assistive training method possesses the rehabilitation advantages of both end-effector and exoskeleton robots. Table II presents the average results of all subjects, evaluated using RMSE and pearson correlation coefficient (PCC).

In terms of joint angles tracking, the proposed dual-arm method shows higher accuracy and stronger error-control capability than the current end-effector (single-arm) and MIME methods. RMSE is used as a measurement indicator, reflecting the overall deviation of the training angles compared to the demonstration angles. Experimental results show that our method achieves RMSE ranging from 0.81 to 2.41, demonstrating performance nearly consistent with the traction demonstrations. In contrast, the single-arm and MIME methods show higher RMSE, peaking at 24.4 and 26.7, particularly

IEEE Robotics and Automation Letters (RA-L) paper, presented at ICRA 2026, Vienna, Austria. Cite as RA-L paper.

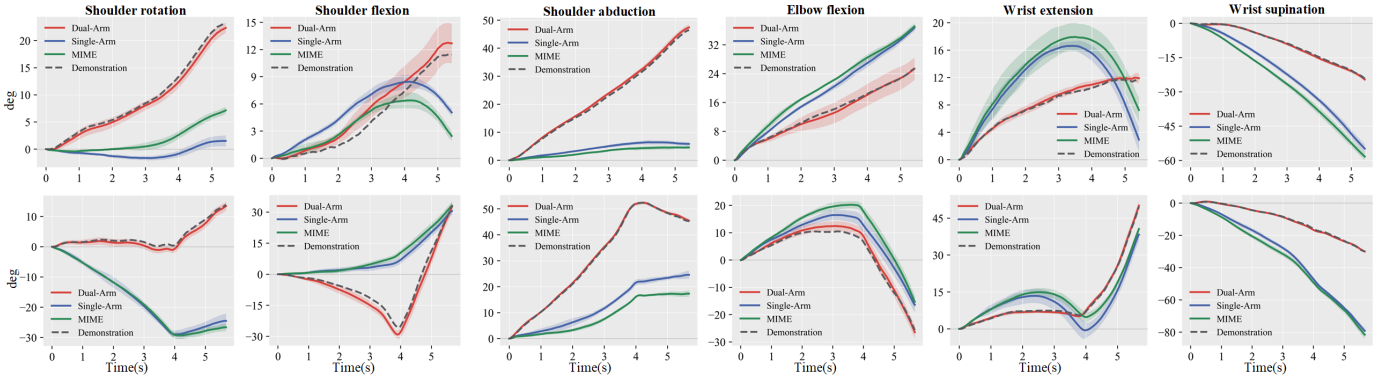

Fig. 7. The first and second rows show joint angle variations during training for motion 1 and motion 2, using subject 5 as an example.

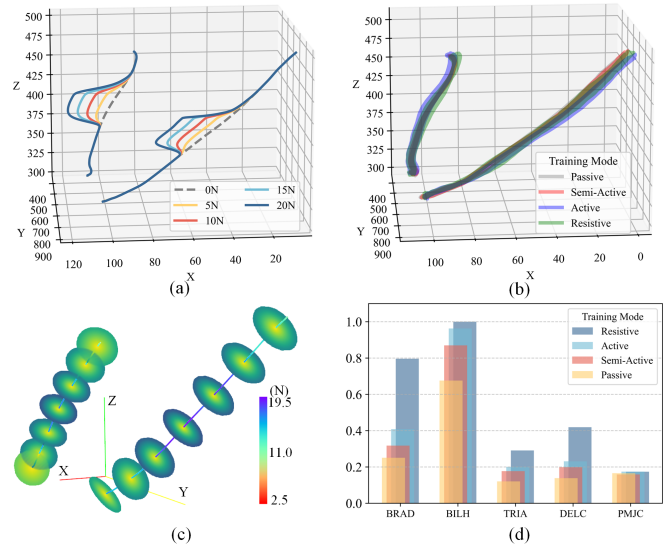

Fig. 8. Multi-mode compliant training. (a) Compliant behavior under different levels of external disturbance force. (b) Comparison of task-space trajectories under four training modes. (c) Visualization of the potential field. (d) Comparison of upper-limb muscle activation under four training modes.

in multi-DOF joints such as the wrist and shoulder. Spatial training under the single-arm and MIME systems shows significant deviations from the demonstrated joint angles, severely compromising training effectiveness and increasing the risk of secondary injury to the affected limb.

In terms of motion consistency and synchronization, PCC provides a correlation measure. For the dual-arm method, the PCC for the shoulder and elbow exceed 0.97, indicating strong temporal tracking of the demonstrated motions and excellent multi-joint coordination control. Even in the relatively complex and highly coupled wrist motions, the PCC remain high (ranging from 0.92 to 1.00), highlighting the dual-arm system's unique capability in capturing fine human motions. The single-arm and MIME methods show low PCC across multiple joints, particularly in shoulder rotation (Single-arm = -0.21, MIME = -0.48) and shoulder flexion (Single-arm = 0.17, MIME = 0.65) during complex Motion 2, and in shoulder flexion (Single-arm = 0.57, MIME = 0.58) and wrist extension (Single-arm = 0.59, MIME = 0.50) during Motion 1. This indicates that joint motion patterns under single-arm and MIME training deviate significantly from the demonstration, posing serious safety risks fo training, especially in high-DOF conditions.

For the single-arm and MIME methods, using robotic arm A for spatial training (Motions 1 and 2) can ensure the endpoint position of the upper limb is correct. However, it fails to accurately control individual joints, leading to substantial deviations in the overall training posture. In comparison, using only robotic arm B for spatial training (Motion 3) improves the tracking accuracy of the shoulder and elbow. However, its control over the distal fine joint remains inadequate, resulting in poor tracking performance and low correlation in wrist motions (PCC: WE = 0.05, WS = -0.91). We randomly choose the result of subject 5 to plot his angle curves. The tracking curves for the rehabilitation Motions 1 and 2 are shown in Fig. 7. Across all rehabilitation motions, the dual-arm method significantly improves joint movement accuracy by increasing assistance from the follower arm. Among them, the dual-arm method exhibits a marked performance improvement over the single-arm and MIME approaches in complex joints such as the wrist and shoulder, indicating its superior capability in executing fine and complex movements. Therefore, compared to other current approaches, the proposed framework demonstrates clear superiority in enabling high-DOF, personalized, and accurate rehabilitation training.

4) Multi-modal compliant training: Fig. 8(c) visualizes the demonstration characteristics during rehabilitation motion 2. The trajectory is color-coded to represent the magnitude of the traction force, ranging from $2.5N$ to $19.5N$. Seven sampled circular cross-sectional planes illustrate the anisotropic attraction distribution of the potential field. In rehabilitation, patients often exhibit abnormal motions such as tremors and spasms. To evaluate the robustness of the system, a disturbance experiment with different levels of abnormal motion is conducted, as shown in Fig. 8(a). Under disturbances of $5N$, $10N$, $15N$, and $20N$, the maximum displacement of the upper limb is 4.9-5.8mm, 10.2-11.5mm, 15.5-17.3mm, and 21.0-23.2mm, respectively. These results indicate that when a disturbance is applied, the upper limb deviates from the trajectory until the restoring force generated by the potential field balances the external force, resulting in a stable maximum deviation. Notably, under the same disturbance, the maximum displacement is not fixed but adaptively varies with the system's variable stiffness at different stages of the demonstration, reflecting its capa-

IEEE Robotics and Automation Letters (RA-L) paper, presented at ICRA 2026, Vienna, Austria. Cite as RA-L paper.

bility for dynamic compliance adjustment. This mechanism effectively limits the range of deviation, thereby enhancing training safety, while also providing greater flexibility by no longer restricting motion to a single fixed trajectory. When the disturbance is removed, the potential field guides the upper limb smoothly back to the desired trajectory, demonstrating the system's excellent clinical robustness, interactive compliance, and safety under disturbances of varying levels.

To match the training intensity with the patient's fatigue level or motor ability, we set four training modes: passive ($F_T = F_{in}$), semi-active ($F_T = 0.5F_{in}$), active ($F_T = 0$), and resistance ($F_T = -0.5F_{in}$), with five reciprocating motions performed in each mode. As shown in Fig. 8(b), the average upper-limb offset distances in each mode are $1.5mm$, $2.7mm$, $4.0mm$, and $4.7mm$, respectively. The passive training and semi-active training trajectories are almost completely consistent, indicating that the system has strong tracking performance on the training trajectory under the assistance condition. The active training trajectory is slightly offset, reflecting that there is a certain degree of compliance in the subject's autonomous movement control under the unassisted state. The resistance training and active training offsets are similar, indicating that the subject is able to maintain stable movement control under resistance. The above results show that the rehabilitation system can achieve good compliance and control stability in multiple interaction modes, and is capable of delivering intensity-adjustable personalized rehabilitation tailored to the patient's condition. The muscle activation patterns observed during the four training modes align well with their biomechanical demands. As shown in Fig. 8(d), the BILH exhibits the highest activation across all training modes, consistent with its key role in controlling elbow flexion and assisting upper limb extension during the chest expansion. The BRAD also shows substantial activation, supporting wrist stabilization and fine motor control. In contrast, muscles such as the TRIA, DELC, and PMJC show lower activation, indicating their supportive roles in maintaining shoulder stability and coordinating multi-joint movements. Therefore, the proposed dual-arm rehabilitation scheme effectively induces muscle engagement consistent with physiological motor control principles, proving its biological rationality and scientific validity in training.

V. Conclusion

In this letter, we propose a therapist-inspired dual-arm rehabilitation framework and validate its effectiveness. Results demonstrate that the framework can effectively learn from both external traction behaviors and internal interaction characteristics, and can be extended to multiple rehabilitation modes, enabling therapist-like safe, scientific, and compliant training. Among them, the dual-arm traction experiments show that the framework has the characteristics of strong individual and motion adaptability and simple wear of the end-effector robots and fine spatial training of the exoskeletons, thereby addressing the limitations of both rehabilitation robot types. Finally, its personalized rehabilitation capabilities and biological rationality are validated through multi-mode compliant training. Future work will focus on advancing clinical trials, validating the clinical rehabilitation effects through physiological signals, and deploying the system on humanoid platforms to promote home-based rehabilitation.

References

[1] V. L. Feigin, M. Brainin, and B. Norrving, "World stroke organization (wso): global stroke fact sheet 2022," *Int. J. Stroke.*, vol. 17, no. 1, pp. 18–29, 2022.

[2] X. Song, "Activities of daily living-based rehabilitation system for arm and hand motor function retraining after stroke," *IEEE Trans. Neural Syst. Rehabil. Eng.*, vol. 30, pp. 621–631, 2022.

[3] J. Dobe and L. Gustafsson, "Co-creation and stroke rehabilitation: A scoping review," *Disabil. Rehabil.*, vol. 45, no. 3, pp. 562–574, 2023.

[4] R. Feingold-Polak and O. Barzel, "Socially assistive robot for stroke rehabilitation: a long-term in-the-wild pilot randomized controlled trial," *IEEE Trans. Neural Syst. Rehabil. Eng.*, vol. 32, pp. 1616–1626, 2024.

[5] S. Han, H. Wang, and H. Yu, "Human–robot interaction evaluation-based aan control for upper limb rehabilitation robots driven by series elastic actuators," *IEEE Trans. Robot.*, vol. 39, no. 5, pp. 3437–3451, 2023.

[6] C. Wang, L. Peng, and Z.-G. Hou, "A control framework for adaptation of training task and robotic assistance for promoting motor learning with an upper limb rehabilitation robot," *IEEE Trans. Syst. Man Cybern.*, vol. 52, no. 12, pp. 7737–7747, 2022.

[7] C. Xie, Y. Lyu, and G. Li, "A cable-driven upper limb rehabilitation robot with muscle-synergy-based myoelectric controller," *IEEE Trans. Robot.*, vol. 40, pp. 3199–3211, 2024.

[8] M. Najafi, C. Rossa, and K. Adams, "Using potential field function with a velocity field controller to learn and reproduce the therapist's assistance in robot-assisted rehabilitation," *IEEE-ASME Trans. Mechatron.*, vol. 25, no. 3, pp. 1622–1633, 2020.

[9] J. Pan, D. Astarita, and A. Baldoni, "Nesm-γ: An upper-limb exoskeleton with compliant actuators for clinical deployment," *IEEE Robot. Autom. Lett.*, vol. 7, no. 3, pp. 7708–7715, 2022.

[10] Y. Zimmermann, M. Sommerhalder, and P. Wolf, "Anyexo 2.0: A fully actuated upper-limb exoskeleton for manipulation and joint-oriented training in all stages of rehabilitation," *IEEE Trans. Robot.*, vol. 39, no. 3, pp. 2131–2150, 2023.

[11] S. E. Ovur and Y. Demiris, "Naturalistic robot-to-human bimanual handover in complex environments through multi-sensor fusion," *IEEE Trans. Autom. Sci. Eng.*, vol. 21, no. 3, pp. 3730–3741, 2023.

[12] D. Sirintuna, I. Ozdamar, and A. Ajoudani, "Carrying the uncarriable: a deformation-agnostic and human-cooperative framework for unwieldy objects using multiple robots," *ICRA*, p. 7497–7503, 2023.

[13] Y. Fan, X. Li, and K. Zhang, "Learning robust skills for tightly coordinated arms in contact-rich tasks," *IEEE Robot. Autom. Lett.*, vol. 9, no. 3, pp. 2973–2980, 2024.

[14] Z. Wang, Y. Gan, and X. Dai, "Assembly-oriented task sequence planning for a dual-arm robot," *IEEE Robot. Autom. Lett.*, vol. 7, no. 3, pp. 8455–8462, 2022.

[15] N. Lv, J. Liu, and Y. Jia, "Dynamic modeling and control of deformable linear objects for single-arm and dual-arm robot manipulations," *IEEE Trans. Robot.*, vol. 38, no. 4, pp. 2341–2353, 2022.

[16] S. Jin and W. Lian, "Robotic cable routing with spatial representation," *IEEE Robot. Autom. Lett.*, vol. 7, no. 2, pp. 5687–5694, 2022.

[17] N. A. Aspragathos and J. K. Dimitros, "A comparative study of three methods for robot kinematics," *IEEE Trans. Syst. Man Cybern.*, vol. 28, no. 2, pp. 135–145, 1998.

[18] J. Zhang and C. C. Cheah, "Passivity and stability of human–robot interaction control for upper-limb rehabilitation robots," *IEEE Trans. Robot.*, vol. 31, no. 2, pp. 233–245, 2015.

[19] S. M. Khansari-Zadeh and O. Khatib, "Learning potential functions from human demonstrations with encapsulated dynamic and compliant behaviors," *Auton. Robot.*, vol. 41, no. 1, pp. 45–69, 2017.

[20] C. G. Burgar, A. E. Scremin, and S. L. Garber, "Robot-assisted upper-limb therapy in acute rehabilitation setting following stroke: Department of veterans affairs multisite clinical trial," *J Rehabil. Res. Dev.*, vol. 48, no. 4, p. 445, 2011.